Experimental Mechanics (2019) 59:643–658
https://doi.org/10.1007/s11340-019-00517-z

Grain Boundary Sliding and Slip Transmission in High Purity Aluminum

M.A. Linne[1] · A. Venkataraman[2] · M.D. Sangid[2] · S. Daly[3]

Received: 8 November 2018 / Accepted: 16 April 2019 / Published online: 23 May 2019
© Society for Experimental Mechanics 2019

Abstract
Despite its significance in polycrystalline materials, there have been few experimental investigations of the activity of grain boundary sliding (GBS) and the relationship between GBS and slip transmission at grain boundaries. The present work addresses this knowledge gap by the characterization of full-field strain and microstructural information in an experimental system of high-purity (99.99%) columnar aluminum subjected to uniaxial tension at 190 °C. High-resolution, full-gage strain fields were characterized on an unloaded specimen by distortion-corrected and stitched scanning electron microscope-enabled digital image correlation (SEM-DIC). Alignment between the lower-resolution electron backscatter diffraction (EBSD) and higher-resolution strain fields was significantly improved by clustering of strain data within an EBSD-defined boundary mantle. Grain boundary sliding was investigated at select boundaries, and it was determined that GBS magnitude profiles can have large gradients along a single boundary and vary significantly between boundaries. Using a geometric compatibility factor (m′) to quantify favorability of slip transmission, the two grain boundaries that exhibited the largest average GBS magnitude experienced contiguous slip on moderately well aligned slip systems, although the exact nature of this slip activity, whether transmission or nucleation, remains under investigation.

Keywords Grain Boundary Sliding · Slip Transmission · Digital Image Correlation · Aluminum · Columnar Microstructure

Introduction

In polycrystalline materials, grain boundaries tend to be areas of strain localization and damage initiation; grain boundaries can obstruct or transmit dislocation motion and can relieve stress via grain boundary sliding (GBS). Both GBS and slip transmission are mechanisms that lead to damage formation in the grain boundary vicinity, and are therefore of interest in understanding and predicting plastic deformation behavior. Dislocation-grain boundary interaction can be characterized by four general cases that can occur when dislocations are incident at a grain boundary, as described by Sutton and Balluffi [1]: *(1) direct transmission, no boundary residual* - the dislocation slips through the grain boundary into the adjacent grain with no residual dislocations remaining in the boundary, requiring cross slip of a screw dislocation at the boundary; *(2) direct transmission with boundary residual* – the slip planes of the incoming and outgoing dislocations intersect at a line at the boundary, but the Burgers vectors differ, so a residual dislocation is left in the boundary; *(3) indirect transmission* - dislocation impingement and emission into the adjacent grain occur on slip planes that do not intersect along a line at the grain boundary plane, also resulting in a residual Burgers vector; and *(4) no transmission* – the incoming dislocation dissociates in the grain boundary, with no dislocation emitted into the adjacent grain. Each of these cases has been observed in experimental studies that have informed the development and served as validation of criteria for predicting slip transmission behavior [2–5].

Atomistic simulations have been used to investigate grain boundary-dislocation interactions (please see [6] and the references contained therein). These approaches have clarified transmission criteria by investigating the atomic-scale mechanics occurring during slip transmission. Molecular dynamics simulations have provided fundamental insights into grain boundary-dislocation interactions, including the stress and

✉ S. Daly
samdaly@ucsb.edu

1 Department of Materials Science and Engineering, University of Michigan, 2300 Hayward St, Ann Arbor, MI 48109, USA

2 School of Aeronautics and Astronautics, Purdue University, 480 W Stadium Ave, West Lafayette, IN 47907, USA

3 Department of Mechanical Engineering, University of California at Santa Barbara, 503 Lagoon Rd, Santa Barbara, CA 93106, USA

grain size threshold for transition from dislocation-mediated to grain boundary-mediated deformation in nanocrystalline materials [7], relative contributions of GBS and intragranular slip to global strain [8], relationship between grain boundary type and energy barrier for slip transmission [9] and the correlation between residual burgers vector and energy barrier to slip transmission [10]. However, computational limitations preclude the atomistic modelling of large polycrystalline microstructures, therefore inhibiting the capture of possible long-range microstructural effects. Additionally, the gap between length scales achievable in these simulations and in experimental approaches makes direct validation of computational results difficult.

In contrast to slip transmission, the fundamental mechanisms resulting in GBS – described as the relative shear displacement between two adjacent grains – are less well understood. These phenomena are typically examined in studies involving creep and testing at elevated temperature (~$0.5T_m$) [11, 12] and in investigations into the deformation of nanocrystalline and ultrafine-grained materials [13, 14]. For a detailed review of past GBS studies, please see [15]. It is postulated that grain boundary dislocations play a role in enabling GBS through a combination of glide and climb in the boundary, the latter of which depends on intergranular diffusion and therefore temperature. Supporting this theory are observations of increasing GBS activity with increasing temperature [16, 17]. The contribution of GBS to total plastic deformation is also sensitive to grain size. It has been observed in 99.995% Al that below a critical grain size, defined by the size of the sub-grains formed during creep and typically less than 10 μm diameter, GBS accounted for essentially all observed plastic behavior during creep at elevated temperature [16]. Additionally, there is computational and experimental evidence that GBS plays a significant role in the room temperature deformation of nanostructured materials with nanocrystalline [13, 18–20] or super plastically deformed [21–23] microstructures.

Experimental investigations of GBS have used fiducial lines at grain boundaries [24, 25] and interferometry to capture in-plane or out-plane sliding respectively, and to thereby approximate the contribution of GBS to total specimen strain [15]. These methods have been used to characterize the globally averaged GBS behavior, but are not able to characterize local microscale changes in GBS activity. Towards this end, transmission electron microscopy (TEM), atomic force microscopy and molecular dynamics simulations have been used to investigate GBS with respect to the local microstructure. However, due to computational and experimental constraints, these studies are performed over small, typically sub-micron fields of view. More recently, researchers have employed DIC to measure full-field GBS displacements [23, 26–28], and have developed crystal plasticity models sensitive to GBS and other physical phenomena [28, 29].

There is increasing evidence that slip transmission and grain boundary sliding are related, but the nature of this relationship - whether synergistic or competitive - remains under debate. GBS can promote slip transmission by relieving stress caused by dislocation pile ups or by the build-up of grain boundary residual dislocations resulting from dislocation-grain boundary interaction [1]. Additionally, the necessary increase of shear stress on a grain boundary for GBS lowers the energy barrier for slip transmission [10]. Valiev et al. [25] experimentally observed a positive correlation between intragranular slip activity and the rate of GBS, in a study of Zn bicrystals loaded at 50 °C. Each Zn bicrystal contained a [12–2 0] 90 deg. tilt boundary ($\Sigma > 25$), with two loading configurations: boundary normal oriented 45 deg. (type I) and 30 deg. (type II) from the tensile axis. The observed GBS rate and magnitude was greater for the type II specimen, which exhibited both GBS and intragranular slip, while the type I specimen exhibited what was deemed 'pure' GBS with no intragranular slip. The authors suggested that this could be due to slip transmission acting as a type of recovery mechanism for hardening caused by grain boundary dislocation pile-ups during GBS, by leaving mobile residuals in the boundary that can facilitate further GBS. While these results suggest that GBS and slip transmission act collaboratively, only one bicrystal boundary type under several different loading cases was studied. Bieler and Mukherjee observed significant GBS during the superplastic deformation of mechanically alloyed IN90211, but determined that intragranular dislocation glide and arrival at grain boundaries, rather than GBS, was deformation rate limiting. This suggests a dependency of GBS on intragranular slip and that arrival and absorption of extrinsic dislocations at grain boundaries helps facilitate GBS [30]. Conversely, Horton [31] observed an increase in GBS rate with decreased intragranular slip, by measuring fiducial scratch displacement and therefore changes in the activity of both mechanisms in Al bicrystals with varying temperature, stress, and Cu impurities. These opposing conclusions, where GBS has been observed to be related to both increasing and decreasing intragranular slip activity, highlight the lack of clear understanding about this mechanism relationship.

There are few mesoscale experimental studies that characterize GBS-slip interactions, which are affected by many different variables including temperature, stress state, impurity content, and local microstructure [14, 23, 26]. While TEM studies [14] and atomistic simulations [8] have greatly contributed to the understanding of fundamental plasticity mechanism interaction near grain boundaries, they focus on very small fields of view, limiting the ability to study longer-range effects as well as to analyze statistically significant numbers of grain boundaries. With recent improvements in spatial resolution and its application under scanning electron microscopy, digital image correlation (DIC) is a powerful tool for investigating this mesoscale bridge, through the full-field strain

measurement and statistical analysis of grain boundary deformation activity. In a recent study, Bourcier et al. [26] measured full-field deformations in halite with varying grain size distributions using both macro- and microscale DIC. Full-field strains were used to calculate the contribution of intragranular slip and GBS to global strain. While the authors acknowledge simultaneous operation of both mechanisms and used 2D strain fields to quantify activity of each, possible dependencies between the two were not explored. Additionally, the contribution from GBS was not quantified by direct measurement, but rather it was assumed that GBS accounted for the remaining strain not measured in intragranular deformation. If other mechanisms, like boundary migration, are active but not considered, then this method could overestimate the contribution from GBS.

In this work, a combination of scanning electron microscopy and digital image correlation (SEM-DIC) was used with grain orientation mapping to examine the full-field microscale deformation in high-purity (99.99%) columnar aluminum subjected to uniaxial tension at 190 °C. High-resolution deformation maps were captured across mm-scale fields of view, enabling the investigation of plastic deformation mechanisms, both sub-grain and at grain boundaries, across the entire gage section of the test specimen. The experimental and analytical methodologies that were created to capture this data will first be described and then demonstrated on the examination of the spatial distribution of GBS along the grain boundary, and of the interaction between slip transmission across a boundary and the average magnitude of GBS.

Experimental Methods

High purity (99.99%), columnar aluminum with specimen dimensions as shown in Fig. 1 was loaded in uniaxial tension at 190 °C. Full-field high-resolution microscale strain and grain orientation information was collected using stitched SEM-DIC and electron backscatter diffraction (EBSD), respectively. Full-field deformation data was collected to investigate the interaction between GBS and slip transmission. This temperature was chosen to increase GBS activity while not initiating dynamic recrystallization (DRX), which would alter the through-thickness grain structure. For a thorough review of DRX and the parameters that influence its activity, please refer to [32]. In brief, although high purity tends to decrease the DRX temperature, the high stacking fault energy and large grain size (~300–1000 μm diameter) of the test specimen favored other recovery mechanisms besides DRX. The testing temperature of 190 °C was considered fairly conservative, as past studies have identified DRX temperatures of 350–450 °C for high purity Al with various microstructures [33, 34]. The absence of observable DRX was confirmed by pre- and post- EBSD characterization.

Aluminum Specimen Preparation

Columnar, high-purity (99.99%) aluminum was chosen for this investigation. In addition to being of interest for lightweight structural applications, Al has an fcc crystal structure and a high stacking fault energy that reduces deformation complexity with minimal twinning. A high purity specimen enabled the examination of grain boundary-dislocation interactions with minimal effect from impurities. A columnar specimen was chosen to minimize subsurface ambiguity of EBSD characterization. Due to this high purity and columnar microstructure, the specimen was extraordinarily delicate and required special consideration during handling, mounting, polishing, EBSD characterization, and subsequent testing. However, this combination of features enabled the collection of a full-gage data set, wherein GBS behavior could be cleanly examined.

Aluminum sheet of 99.99% purity and 0.5 mm thickness was obtained from EPSI Metals and annealed at 550 °C in argon for six hours to produce large grains with a partially columnar grain structure that was confirmed by EBSD on both specimen faces, as shown in Fig. 2. Figure 2(a) and 2(b) show the front and back inverse pole figure maps for out-of-plane (a3) and tensile axis (a2) directions respectively. In Fig. 2(c), the front (black) and back (gray) [001] pole figures are

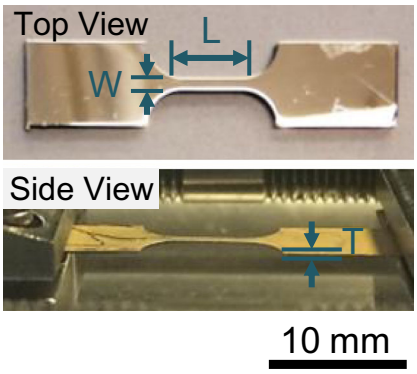

Gage Dimensions	Size (mm)
length (L)	5.0
width (W)	1.0
thickness (T)	0.36
Test Parameter	**Value**
image resolution (μm/pix)	0.082
speckle diameter (μm)	0.3
total fields of view	60 (4x15 array)

Fig. 1 Specimen dimensions and DIC parameters

superimposed, with the poles from the latter rotated 180° about the a1 axis. If perfectly columnar, the pole figures would match. The specimen was not perfectly columnar, as there are grains near the edges of the specimen gage that do not appear to extend through the specimen thickness (grains a-i in Fig. 2(a)). A detailed analysis of specimen microstructure and columnarity is discussed in Online Resource 1. The tensile specimen with a 5 × 1 mm^2 gage area was cut from the sheet using wire electric discharge machining and mounted to an aluminum holder using a thin adhesive layer (crystalbond 509 and acetone, 1:4 wt mixture). It was then manually polished using 600 grit, 800 grit, and 4000p SiC paper (Buehler CarbiMet and MicroCut), followed by 3 μm and 1 μm polycrystalline diamond paste (Buehler MetaDi Ultra Paste) and finished with a final abrasive 0.05 μm colloidal silica solution (Buehler MasterMet 2) using a vibratory polisher (Pace Technologies, GIGA-0900). The resulting specimen thickness after polishing both sides was 0.36 mm. The specimen was rinsed, while still mounted to the aluminum holder, using deionized water and soap (Simple Green All-Purpose Cleaner) to remove residual colloidal silica. The specimen was soaked in acetone for several hours to dissolve the adhesive and to remove the test specimen from the aluminum holder. The specimen was then placed in fresh acetone for three soak cycles of five minutes each, until the specimen surface appeared free of adhesive by visual inspection. The specimen then was soaked in isopropanol (three soak cycles of five minutes each) to remove acetone residue. Two 40 × 40 μm^2 fiducial markers were placed every 1.67 mm along both edges of the specimen gage (eight markers total), using e-beam platinum deposition in a scanning electron microscope (FEI Teneo). The four corner markers were used to align strain fields and EBSD maps; an affine transformation was applied to the EBSD data, using the fiducial markers as control points to align both orientation and strain arrays. Full-gage grain orientation data was collected via EBSD using an EDAX Hikari EBSD camera and FEI Teneo scanning electron microscope. This process was repeated on the second side of the specimen as shown in Fig. 2.

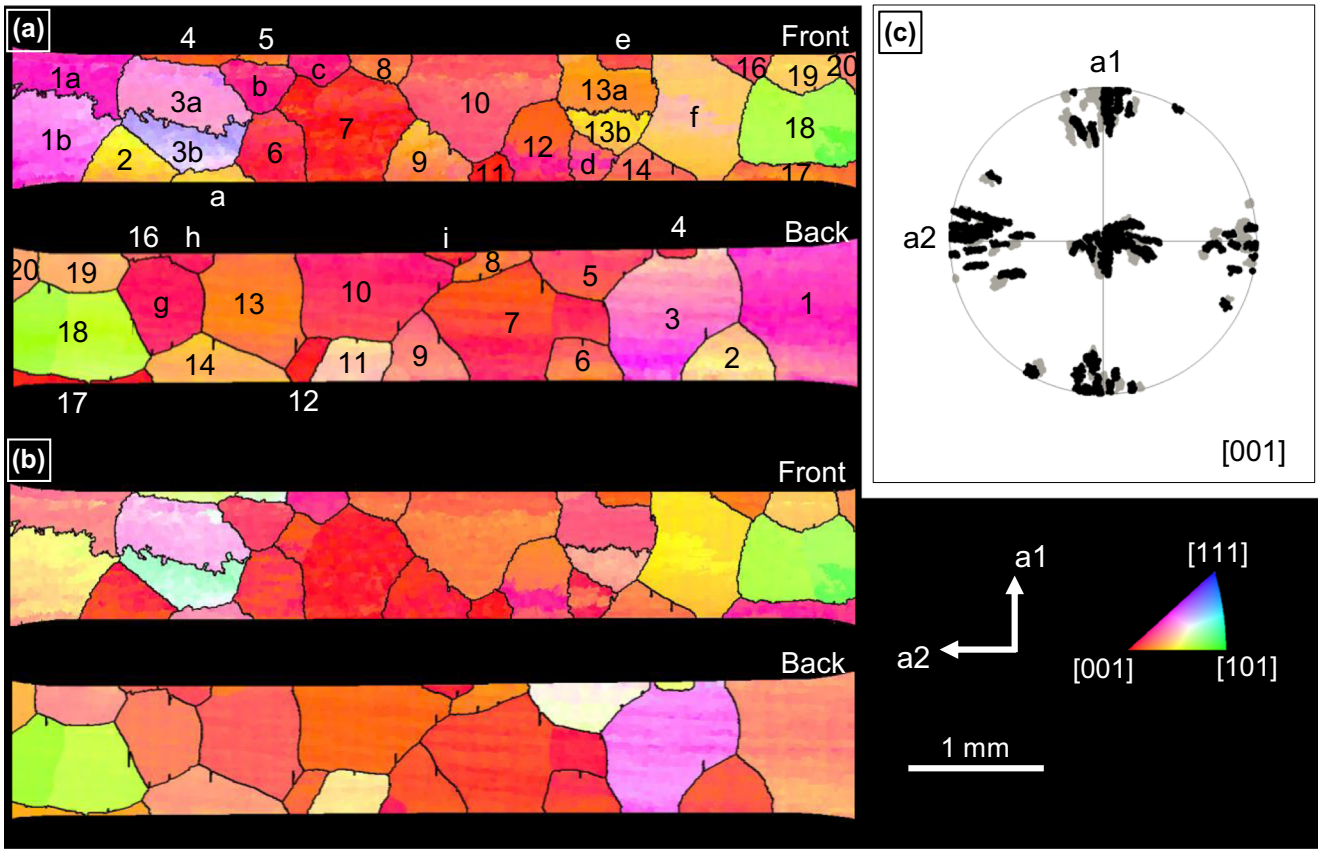

Fig. 2 (**a**) Sample normal direction inverse pole figure maps of the front and back of the full Al specimen gage, showing partial evidence of the same grain orientation on both sides indicating that most grain boundaries are columnar. Corresponding grains on both surfaces are labeled with numbers while non-through-thickness grains are labelled with letters. (**b**) Inverse pole figure in tensile axis (a2) direction and (**c**) [001] pole figures for front and back specimen surfaces are superimposed. The front and back pole figures are plotted in black and gray respectively, with the poles from the latter rotated 180° about the a1 axis

Speckle Patterning for SEM-DIC with Gold Nanoparticles

Gold nanoparticles (AuNPs) of 300 nm diameter, stabilized in citrate buffer, were purchased from Sigma Aldrich and chemically attached to one side of the specimen to produce a random, evenly distributed speckle pattern suitable for collecting high-resolution microscale strain fields with SEM-DIC. An example of this nanoparticle pattern is shown in Fig. 3. Note that there is some agglomeration of the nanoparticle pattern, but the individual AuNPs were resolved at the length scale relevant to the correlation subset size as shown in the magnified view of the pattern in Fig. 3. The AuNPs were applied using a surface silanization technique developed in [35]. The following silanization procedure was used: (1) specimens were cleaned by soaking in isopropanol for ten minutes, followed by soaking in deionized water for ten minutes, and then removed to air dry; (2) subsequently, 50 mL deionized water and 50 mL ethanol were mixed in a 500 mL crystallizing dish with a stir bar for forty minutes; (3) 2.5 mL (3-aminopropyl)trimethoxysilane (APTMS) was then added in approximately 0.1 mL-sized droplets, while stirring for 10 min; (4) the test specimen was then positioned horizontally in the solution, with the side to be patterned facing up. This was carefully done using a sling made from aluminum foil, shown in Fig. 4, which held the specimen while soaking in APTMS solution. Without this device, which supports the back face of the specimen, the delicate specimen was prone to bending upon removal from the solution due to liquid surface tension; (5) the specimen was soaked for 20 min with the solution continuously stirred, and then removed and rinsed with ethanol followed by deionized water for five seconds each. While rinsing, the specimen was supported from the back side by placing it against an aluminum holder to prevent bending.

After the specimen had air dried, 25 mL of the 300 nm AuNP solution (Sigma-Aldrich) was poured into a 50 mL beaker and agitated for 5 min in an ultrasonic bath (FS20H, Fisher Scientific) to stir the settled AuNPs into a suspension. The specimen was submerged using a new aluminum foil sling, which was not exposed to APTMS, and positioned horizontally with the side to be patterned facing upwards. The silanized sling used in the previous step was not reused in this step because the sling is prone to attach to the AuNPs and significantly reduce the specimen pattern density. Due to their relatively large size, the 300 nm AuNPs settled quickly, causing the solution to look clear with orange residue at the bottom of the vial. Therefore, every twenty minutes the specimen was removed and the solution was agitated for several minutes until it once again appeared cloudy orange, indicating AuNP suspension, and the specimen was replaced. This process was repeated three times to increase AuNP attachment density. The specimen was then removed, rinsed for ten seconds with deionized water, and gently blown dry with house air while the specimen was again supported on its back face by an aluminum holder.

Tensile Testing

Before thermo-mechanical straining, a full microstructural map of the specimen gage was captured by EBSD. Following this, the specimen was patterned with AuNPs using the procedure described above, and a series of calibration images for SEM-DIC were collected in-SEM for the full specimen gage following the procedures of [35–37] and later used to correct for SEM distortions. SEM-DIC reference images were collected in a 4 × 15 array of overlapping fields of view (FOVs), each with 82 nm/pixel resolution, that were stitched together post-test to cover the 1 × 5 mm^2 specimen gage

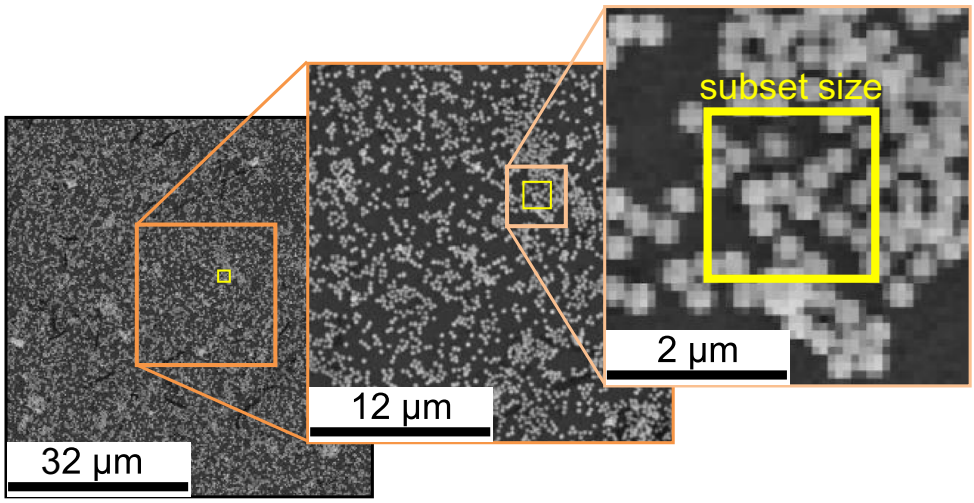

Fig. 3 Gold nanoparticles were applied using the surface silanization technique of [35] to serve as a speckle pattern suitable for SEM-DIC. The correlation subset size (21 × 21 pixels) is shown at three image magnifications for comparison with speckle pattern size and image resolution

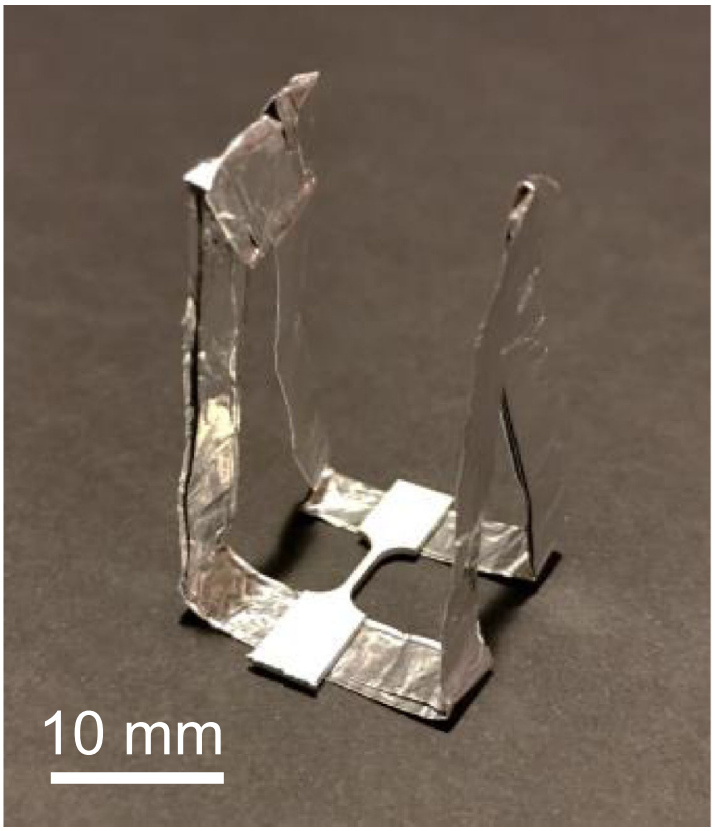

Fig. 4 An example of the aluminum foil sling used in the nanoparticle speckle pattering process, holding a dummy specimen. Different slings were used for the silane and gold nanoparticle solutions. The specimen remains on the sling while submerged in either solution, so the specimen can be easily removed without having to be removed, and possibly damaged, by manipulation with tweezers

section. The FOVs in the reference image array were collected with 20% overlap in the direction of the applied load to prevent loss of gage information due to specimen elongation. The microstructural array was comprised of approximately 400 individual EBSD scans that were stitched together using commercial software (TSL OIM 7, EDAX). The strain data array contained 43.5 million (2900 × 15,000) data points across 60 FOVs that were stitched using custom software to cover the entire 1×5 mm^2 gage section. The 60 FOVs were correlated separately using commercial DIC software (Vic2D 6, Correlated Solutions) using a step size and subset size of 5 pixels and 21 × 21 pixels respectively. These fields were then corrected for SEM distortions and stitched following [38]. The selected correlation step size resulted in a pixel resolution of the displacement fields of 0.41 μm/pixel.

Samples were strained *ex-situ*, while heated to 190 °C, using a tension-compression stage (Kammrath and Weiss), following which the specimen was unloaded for plastic deformation mapping in a FEI Teneo SEM. The oxide layer formed on the tensile specimen during *ex-situ* heating at this temperature is expected to be less than 10 nm thick [39, 40], which is four orders of magnitude thinner than the specimen thickness (360 μm) and not expected to significantly affect mechanical behavior. With the tension-compression stage outside of the SEM, the specimen was heated to 190 °C and strained with a globally applied rate of $\dot{\varepsilon} = 2 \times 10^{-4}$ s^{-1} to a set strain increment (ε^G), at which point the specimen was unloaded, allowed to cool, and transferred to the SEM for deformation mapping. To avoid damaging the specimen, the experimental setup was designed so that the entire tension-compression stage could be transferred between the heating/cooling setup and the SEM chamber without removing the specimen. In Fig. 5 the tension-compression stage is shown mounted in the *ex-situ* setup, on the heating/cooling system. Because the grips in contact with the specimen are non-conductive plastic, a copper clip (seen in Fig. 5) that could be easily attached during in-SEM imaging and removed during *ex-situ* heating and straining, was used to ground the specimen. Deformation maps of the unloaded, cooled specimens were obtained in-SEM at globally-applied strains of $\varepsilon^G = 1.5 \times 10^{-4}$, 5.5×10^{-3}, 0.011, 0.019, 0.028, 0.036, and 0.046. The globally-applied strains ε^G were obtained by measuring gage elongation from stitched SEM images using an image processing program (Image J).

During *ex-situ* testing, the specimen was heated by a resistive heater situated below the specimen. Due to the highly delicate nature of the specimens, a compliant sheet of graphene was used to conduct heat from the heater to the bottom of the specimen. The stage was attached to a water cooling system (Kammrath and Weiss, Caron) to prevent the load cell from overheating, as shown in Fig. 5. Stresses due to thermal expansion were calculated to be on the order of 100 MPa for this specimen geometry, an order of magnitude larger than the expected yield stress of 10 MPa. Therefore, to avoid thermally-induced yielding, the specimen grips were

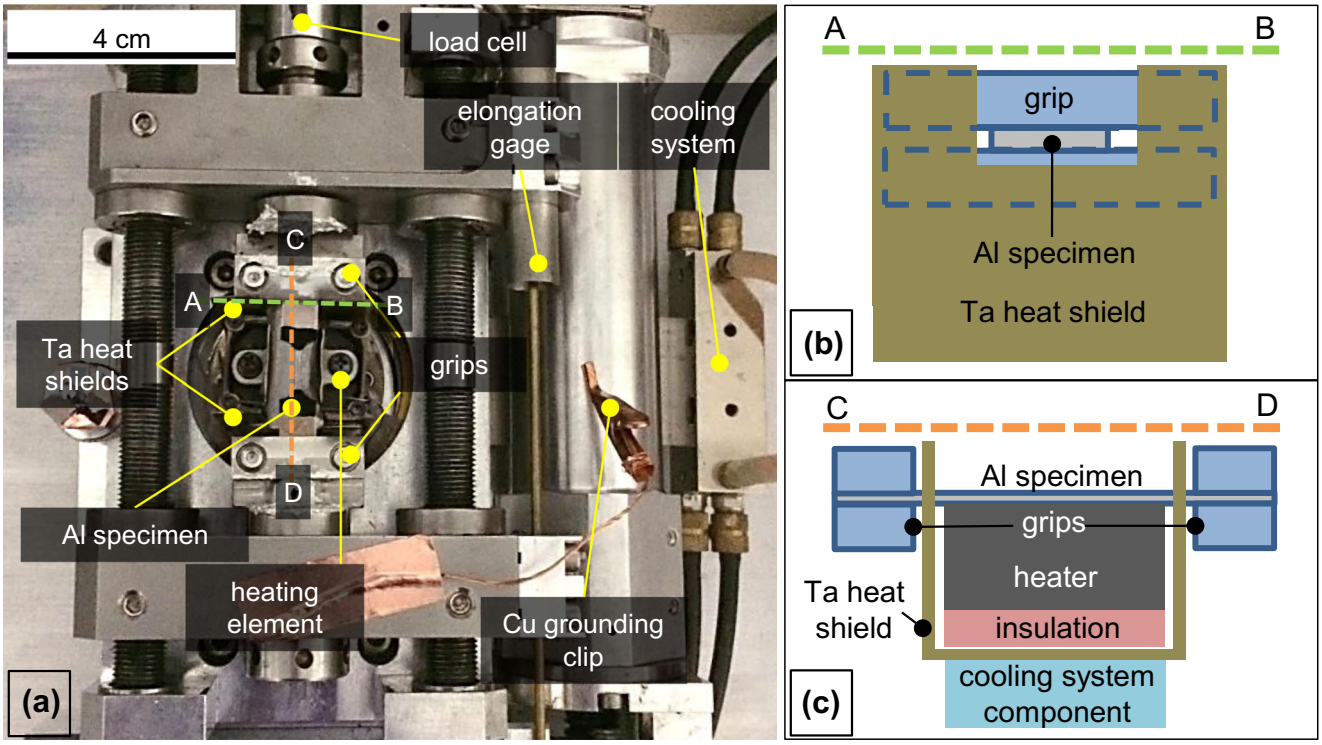

Fig. 5 (**a**) Experimental deformation stage setup for uniaxial testing of 99.99% pure aluminum specimens with through-thickness grain structure at 190 °C, mounted on the heating element and cooling system. Because specimen heating and straining are conducted ex-situ, the setup was designed so that the entire stage could be transferred between the heating/straining setup and mounted in the SEM without removing the specimen. (**b**) and (**c**) are cross-sectional diagrams corresponding to lines A-B and C-D respectively in (**a**). Both (**b**) and (**c**) show the Ta heat shield which reduces radiant heat transfer to the specimen grips. The Ta shield itself is directly attached a component of the cooling system from below via two screws, while the heater and shield are separated by silicone insulation, seen in (**c**)

adjusted during specimen heating and cooling to maintain zero load. Grip adjustment, rather than ungripping the specimen, was used to avoid stress due to thermal expansion because this method posed less risk of damaging the specimen. Note that the cooling rate of the specimen was not constant and grip adjustment was conducted manually. After returning to room temperature, the tension-compression stage holding the test specimen was placed as a unit into the SEM to collect full-gage images.

Results and Discussion

The evolution of the full-field strains at 190 °C is shown in Fig. 6, with the corresponding globally-applied strain (ε^G) and engineering stress (obtained from the 10 N load cell) referenced in the table. Strain fields were stitched following the process outlined in [38]. Deformation trends with respect to microstructural features were identified through the alignment and analysis of the stitched strain and EBSD data arrays. Slip transmission was identified by characterizing slip trace directionality, sequence, and location along the boundary by observing trace evolution in strain fields from increasing global strain increments. While the traces seen in the magnified view of Fig. 6 appear to transmit across the boundary, trace directionality suggests possible boundary nucleation, which highlights the inadequacy of only characterizing boundary-dislocation interaction spatially in a single strain increment; detailed criteria for identifying and classifying transmission activity are discussed in detail in a following section. A magnified view of the yellow boxed boundary from the global strain ε_7 strain field in Fig. 6 is shown in Fig. 7. To investigate the activity of GBS, the relative in-plane displacement tangent to the grain boundary was calculated along the length of the grain boundary from the SEM-DIC strain data. As shown in Fig. 7, this relative displacement between the adjacent grains highlighted the local activity of GBS, which in this case was on the order of five microns.

The assessment of deformation mechanisms close to the grain boundary required accurate alignment of the EBSD microstructure maps and SEM-DIC microscale strain data. Alignment between the lower-resolution EBSD and higher-resolution SEM-DIC fields was significantly improved by clustering strain data within an EBSD-defined boundary mantle. EBSD data is typically of lower spatial resolution than SEM-DIC obtained strain fields, and this resolution disparity can be exacerbated by the need to obtain EBSD

Increment (ε_n)	1	2	3	4	5	6	7
Strain	1.5×10^{-4}	5.5×10^{-3}	0.011	0.019	0.028	0.036	0.046
Stress (MPa)	8.89	8.72	8.00	7.67	8.06	8.36	8.61

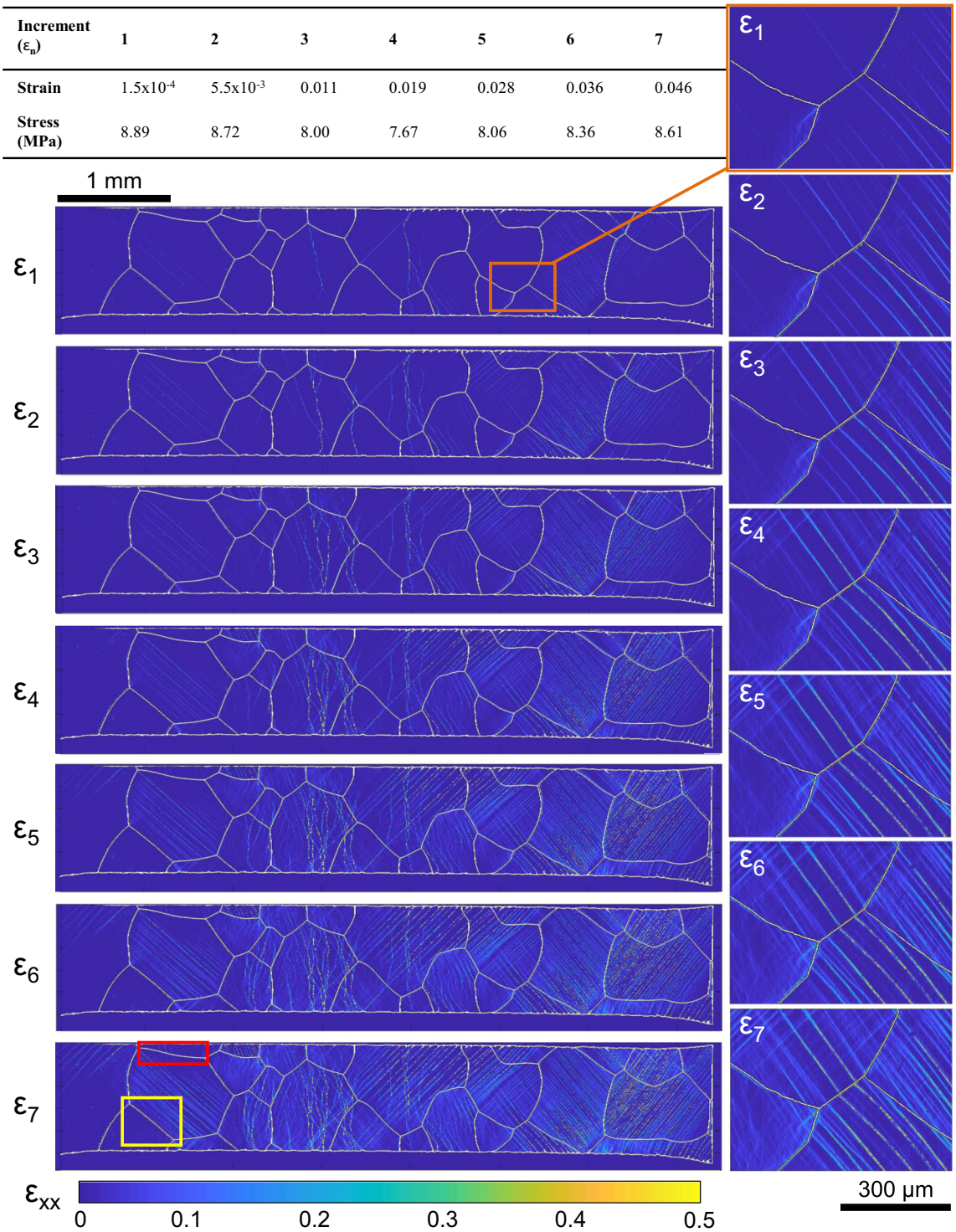

Fig. 6 Full-gage strain evolution from *ex-situ* loading at elevated temperature: (Top Left) Table of the stress and strain where the sample was then unloaded. (Left) Full-gage axial (ε_{xx}) strain fields for each strain increment, with EBSD-identified grain boundaries overlaid. (Right) A select magnified region of the strain field, highlighting the resolution of individual slip bands and evolution of strain localization with increasing global strain. The in-plane GBS profiles for the two boundaries boxed in the (ε_7) strain field are shown in Fig. 10

data over large fields of view in tractable testing times. In this case, a 5 μm step size was used for EBSD to map the entire 1×5 mm^2 gage section. The initial misalignment between the EBSD and SEM-DIC data is shown in Fig. 8 (a). In theory, if GBS is characterized by tangential rigid body displacement (termed here as pure GBS), this error margin should not significantly affect GBS magnitude calculations. However, in cases where GBS is accompanied

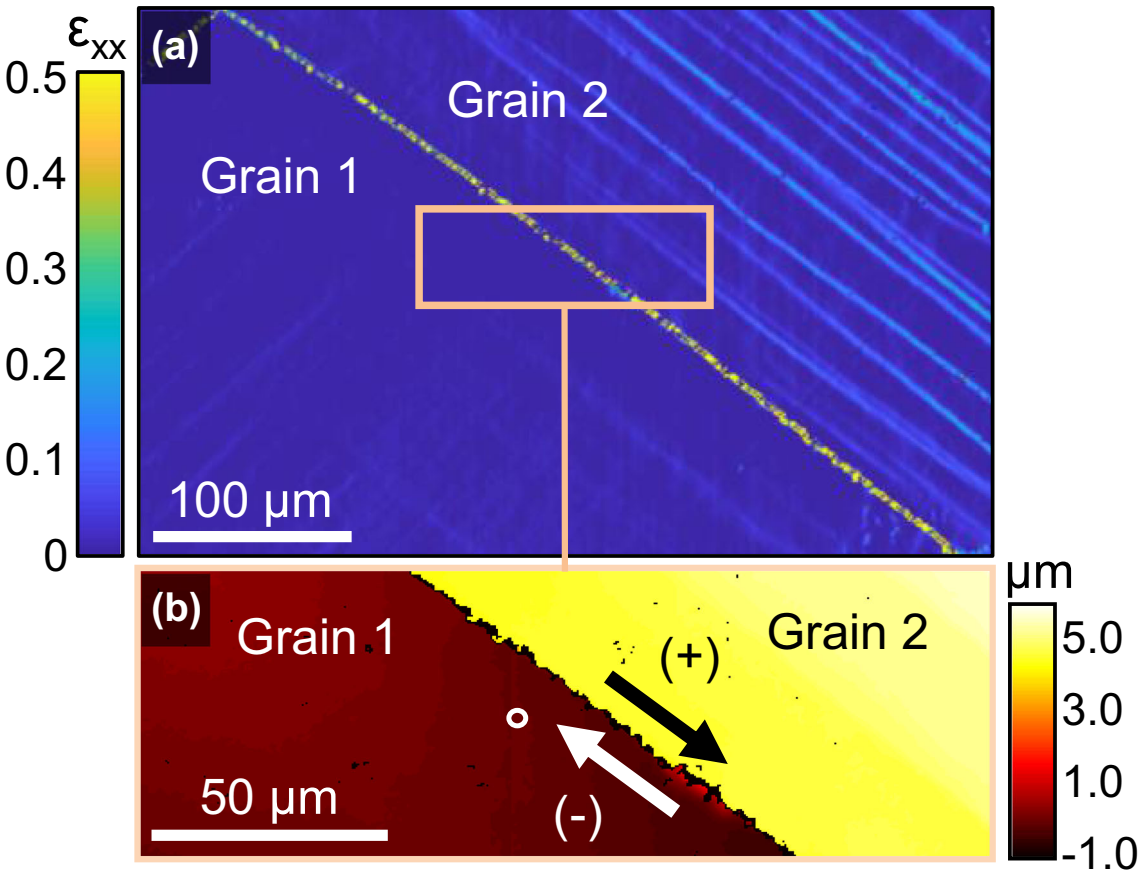

Fig. 7 A selected grain boundary (boxed in yellow in the ε_7 strain field of Fig. 6) is shown to demonstrate quantification of GBS magnitude. (**a**) Local axial strain field (ε_{xx}) at a globally-applied strain of $\varepsilon_7 = 0.046$ indicates strain localization at the grain boundary. (**b**) The relative displacement tangent to the grain boundary is shown for the outlined subset of the area in (**a**). The white circle in (**b**) indicates the reference point used to calculate the tangential displacement field from the DIC displacement fields

by local slip and plasticity observed in the grain boundary vicinity (termed here as simultaneous GBS), the GBS magnitude calculations can vary significantly with distance from the grain boundary (a gradient in shear displacement is evident Fig. 7). In studies where fiducial lines were used, the simultaneous GBS case may manifest as fiducial line bending in addition to a step displacement at the grain boundary [25, 31, 42]. It is understood that slip is often required to accommodate GBS strain in polycrystalline microstructures, and that stress localization at grain boundaries (e.g., due to compatibility stresses or dislocation pile ups) can cause local slip system activation. These cases highlight the importance of characterizing grain boundary-local plasticity, and therefore underline the importance of high-resolution strain measurement and precise grain boundary identification. By clustering and fitting strain points within the vicinity of the EBSD-identified grain boundaries, shown for a selected boundary in Fig. 8 (a), grain boundary identification could be significantly improved as shown in Fig. 8 (b). Details for this alignment procedure are described in [41].

Many image correlation routines use local schemes for displacement and strain calculations, causing a loss of resolution informally referred to as 'smearing' at displacement discontinuities such as slip traces and grain boundaries. These sharp displacement discontinuities can be averaged over a larger pixel width, the magnitude of which depends on correlation parameters [43] amongst other possible factors. For accurate GBS calculations, it was necessary to disregard displacement points within this smeared region, here termed the effective boundary width (EBW). The average EBW for this data set was determined to be approximately 20 pixels (8.2 μm) with the DIC parameters used (5 pixel correlation step size and 21 × 21 subset size). Pixels within this EBW region were disregarded in all GBS magnitude calculations. Local profile disruptions were observed when there was significant misalignment (larger than the EBW) between the EBSD and SEM-DIC data that resulted in the affiliation of displacement points with the incorrect grain. Therefore, tangent displacements involved in calculating GBS magnitude were chosen as close as possible to the identified boundary, while still remaining outside the pixel margin determined by the larger of

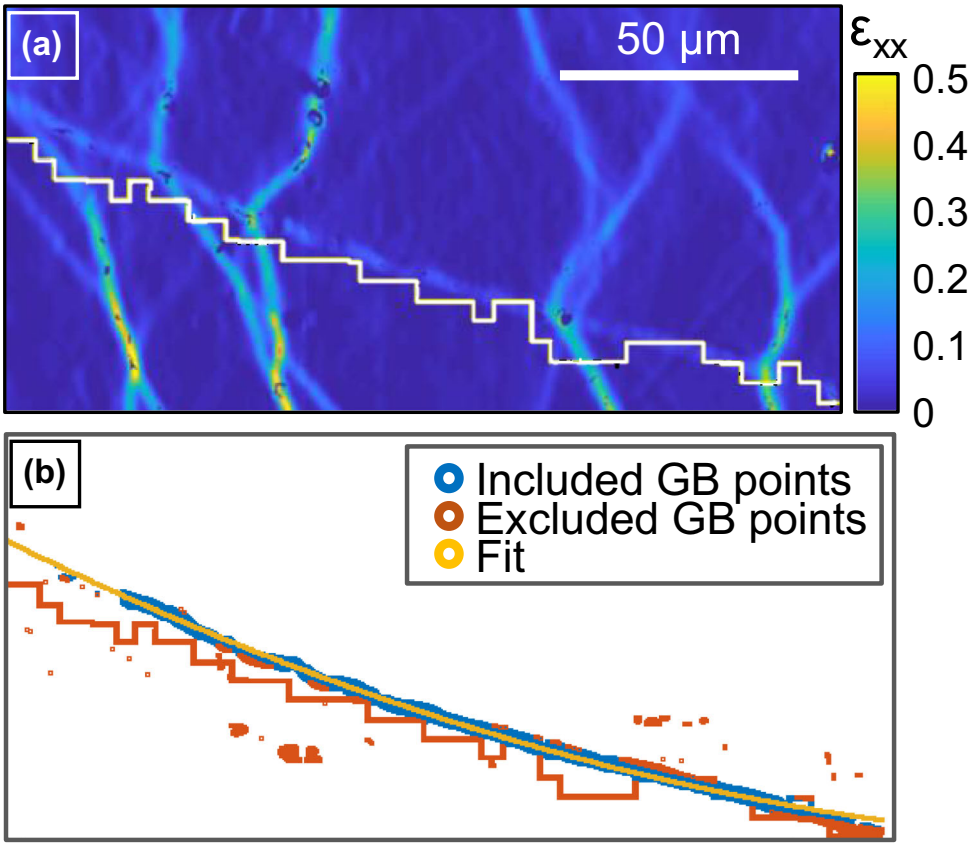

Fig. 8 (**a**) Axial strain field with EBSD-identified grain boundary overlaid, showing evident misalignment. (**b**) To improve alignment, strain data points in the vicinity of the EBSD-identified boundary were identified by k-means clustering and fit using an iterative process that removed outliers using a standard deviation threshold. A plot of the resulting second order polynomial fit after convergence is shown with the grain boundary points included (blue) and excluded (orange) in the final fit. The orange outlying points in (**b**) are local high strain points that were classified as boundary points after k-means clustering, but removed using the iterative fitting process. See [41] for alignment procedure details

the EBW and EBSD-DIC alignment offset. This mantle width varies with DIC and EBSD parameters, and again underlies the importance of precise grain boundary identification. In Fig. 9 and Fig. 10, in-plane GBS magnitude was calculated for grain boundaries identified in red and yellow boxes in Fig. 6 (ε_7), using several different mantle widths to determine parameter sensitivity. For profiles A-B and C-D, average GBS magnitude variation between 10 and 30 pixel widths was 0.0003 and 0.03 μm respectively. There are several factors that can contribute to the sensitivity of the measured GBS magnitude to mantle width variation, including the amount of near-boundary deformation activity and alignment of microstructure and strain data.

Slip activity near or at a grain boundary contributed uncertainty to the calculation of grain boundary sliding that was assessed by averaging the tangential displacements along the boundary. Consequently, as shown in Fig. 9, the grain boundary sliding profiles of boundaries with high slip activity near them exhibited more displacement variation than the grain boundaries with low slip trace activity. In some cases, the clear presence of slip traces along the boundary could be correlated to local jumps in the grain boundary sliding profile, as shown in Fig. 9. Although the displacement contributions from slip traces were local in nature, the spatial averaging of the algorithm used to calculate the GBS magnitude led to sloped jump portions of the GBS profile that varied with the angle between the slip trace and grain boundary. Figure 9 is an example case showing the effect of the slip traces on GBS profile. Four slip traces in the top, seen in the axial strain (ε_{xx}) field in Fig. 9 (a), impinge on the grain boundary. This represents one of the simplest slip-grain boundary interaction cases observed in this specimen: slip traces met the grain boundary from only one side, represented a single slip system, and were spaced far enough apart for the individual tangential displacement contributions to be resolved in the GBS profile. Significant jumps at the locations where slip traces met the grain boundary are evident in the profile along the grain boundary of the in-plane GBS magnitude, as shown in Fig. 9 (b). In order to provide further evidence that these jumps were caused by the contribution from slip impingement, the DIC-measured displacement fields were used to calculate the approximate jump expected in the GBS profile. First, due to both the GBS and slip

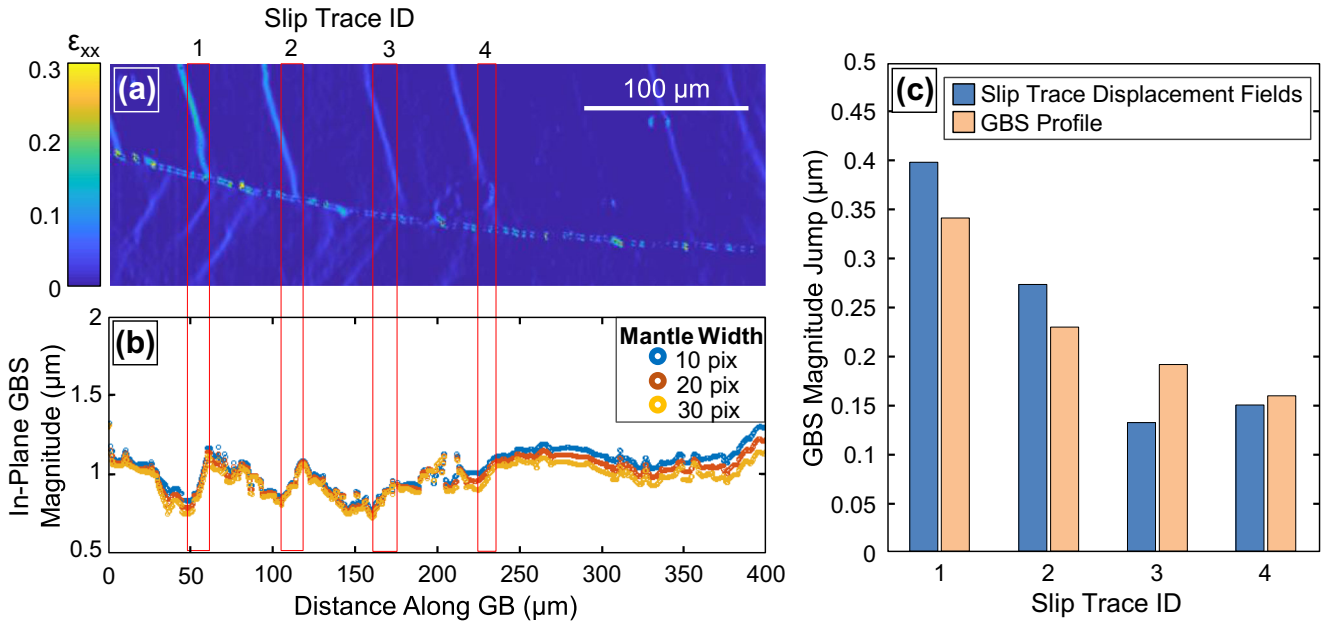

Fig. 9 (**a**) Axial strain field (ε_{xx}) showing an example of slip-grain boundary interaction. Four slip traces meeting the boundary from Grain 1 are identified, showing an increasing displacement trend (**b**) to the left of each trace in the corresponding in-plane GBS profile aligned with (**a**); (**c**) GBS magnitude jumps estimated from slip trace displacement discontinuities (blue bars), and directly measured from GBS profile in (**b**) (light orange bars), are similar for the four highlighted traces

directionality, the observed slip steps were expected to increase the sliding magnitude, because the x and y components of displacement discontinuities due to slip and sliding of the lower grain with respect to the upper grain were both positive. The magnitudes of the GBS profile jumps were estimated by measuring the displacement discontinuity in the slip trace at three random points along each of the four traces. The potential grain boundary-tangent displacement arising from the average displacement resulting from each trace was compared to the jumps identified in the GBS profile, and the magnitudes of both are similar, shown in dark blue and light orange respectively in Fig. 9 (c). Both measurements indicate a similar

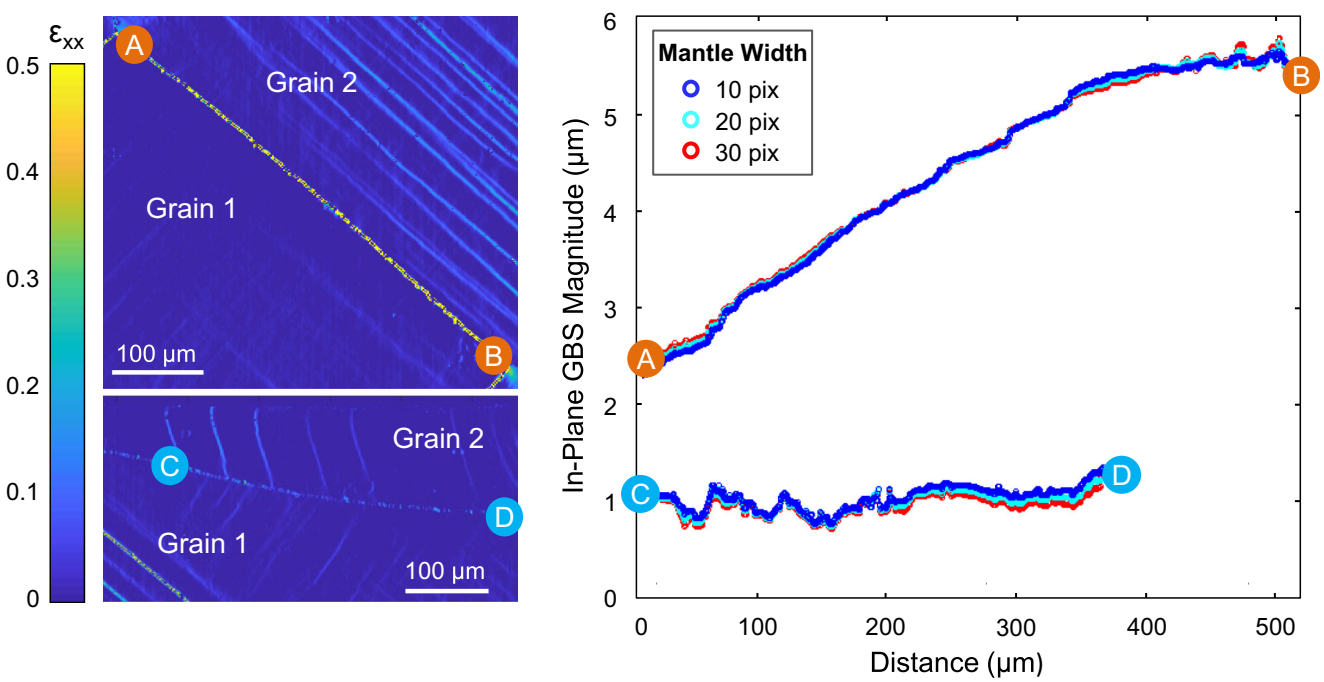

Fig. 10 (Left) Axial strain fields showing two different grain boundaries at a globally-applied strain of $\varepsilon_7 = 0.046$. The upper and lower fields are the same grain boundaries from Fig. 7 and Fig. 9 respectively. (Right) GBS magnitudes for grain boundary lengths between A-B and C-D are plotted for various mantle widths

displacement magnitude, supporting the hypothesis that the highlighted profile steps are a result of local slip activity. While it is difficult to separate slip and sliding contributions in the GBS profiles, especially in more complex local slip cases, the contribution of individual slip traces can be estimated using DIC-measured displacement fields and superimposed onto the GBS magnitude profile. If the estimated slip trace displacement contribution is significantly less than the average GBS magnitude, it can be inferred that there is a large contribution of GBS to grain boundary tangent displacement.

The profile of GBS was spatially-resolved as shown in Fig. 10 for the grain boundary from Fig. 7 (Fig. 10, profile A-B) and Fig. 9 (Fig. 10, profile C-D). The boundary of Fig. 7 had a large (33 deg) misorientation and experienced large resolved shear stress, as the in-plane component of the grain boundary normal was inclined 50 deg. from the tensile axis. Due to the columnar specimen microstructure (observed from the front and back inverse pole figure maps in Fig. 2), the out-of-plane boundary normal component was assumed to be relatively small for this boundary. Based upon this assumption, the boundary normal was angled approximately 5 deg. from the orientation maximizing the macroscopic shear stress (inclined 45 deg. from the tensile axis). These characteristics made this particular grain boundary a strong candidate for GBS. In this instance, the in-plane magnitude of grain boundary sliding was on the order of several microns, and varied approximately linearly along the grain boundary length, shown by Fig. 10, profile A-B. GBS gradients were similarly observed by Mussot et al. [44] and Doquet et al. [28], with the former showing the derivation of GBS sensitive strain compatibility requirements in which the presence of a GBS gradient indicates a mismatch between the grain boundary-tangent strain field components of the adjacent grains.

The profile of GBS varied significantly based on the grain boundary under investigation. For example, this is evident when comparing both profiles in Fig. 10. For profile C-D, GBS stayed relatively constant along the length of the grain boundary compared to the nearly linear increase observed in profile A-B. The relationship of the GBS profile along a boundary to the surrounding microstructure, and its relation to the spatial distribution of slip transmission along the grain boundary, will be investigated in future work.

To relate slip and GBS, the geometric compatibility factor (m′) was used to quantify the ease of slip transmission at each grain boundary. This transmission criterion, employed by Luster and Morris [45], is a measure of how well oriented the incoming and outgoing slip systems are for slip transmission. The m′ value is a product of the cosines of the angles between slip plane normals and burgers vectors. A m′ value of 1 indicates a grain boundary that is transparent to dislocation slip, whereas a m of 0 indicates an impenetrable boundary [45, 46]. Grain boundaries more favorably oriented for slip transmission (m′ > 0.9) exhibited a relatively tighter distribution of grain boundary sliding magnitudes ranging from 0.5–4 μm. This is shown in Fig. 11, which plots the average in-plane GBS magnitude vs. m′ for grain boundaries in the full gage shown in Fig. 6 The most probable m′ value was plotted for boundaries that exhibited clear, identifiable slip activity in both adjacent grains, as determined by examination of the experimentally-obtained trace orientation and ratio of relative x and y displacement discontinuity across slip traces [47]. Three data points, j, k, l, also have a secondary m′ values that could also be probable due to close similarities in slip trace orientation and relative x and y displacement ratio of two possible slip systems.

To characterize the experimentally observed grain boundary-dislocation interaction to compare to the geometric m′ condition, grain boundaries were classified into one of three cases. *Case 1: Transmission* - Boundaries in this group interacted with at least one pair of potential incoming and outgoing traces in adjacent grains (trace pair) that met all the following criteria: (1) the two traces aligned spatially at the boundary, (2) trace pair directionality was appropriate for transmission: one trace was approaching the boundary and the second was moving from the boundary, as confirmed by the DIC strain field evolution under increasing global load, (3) the sequence of trace appearance was consistent with transmission: the identified outgoing trace did not appear before the incoming trace met the boundary. Although there exist other types of boundary-dislocation interactions involving dislocation absorption and emission along different grain boundary locations, they are difficult to identify using *ex-situ* SEM-DIC, and were not considered in the presented analysis. *Case 2: No Transmission* - All boundaries in this group saw local slip activity in both grains, but no trace pair met all criteria for Case 1. Examples include trace pairs caused by dislocation emission from the same boundary location and by boundary emission before the impingement of incoming the dislocation. These two examples, which meet the first criterion for Case 1 and appeared very similar to transmission events in the final strain field, highlight the importance of reviewing all strain increments during classification. *Case 3: Undetermined* - there were three boundaries in this work where one or more of the classification criteria could not be confidently identified. In all of these boundary cases, criterion (1) for Case 1 was met, but traces in the pair seemed to appear simultaneously due to either the low temporal resolution of the experiment, leaving ambiguity with respect to trace sequence, and/or the opposite directions of shear strain along slip traces, determined by the DIC analysis in adjacent grains, suggests dislocation emission from the same boundary location into both grains.

All grain boundaries with m′ > 0.9 showed strong signs of slip transmission. Grain boundaries that experienced no

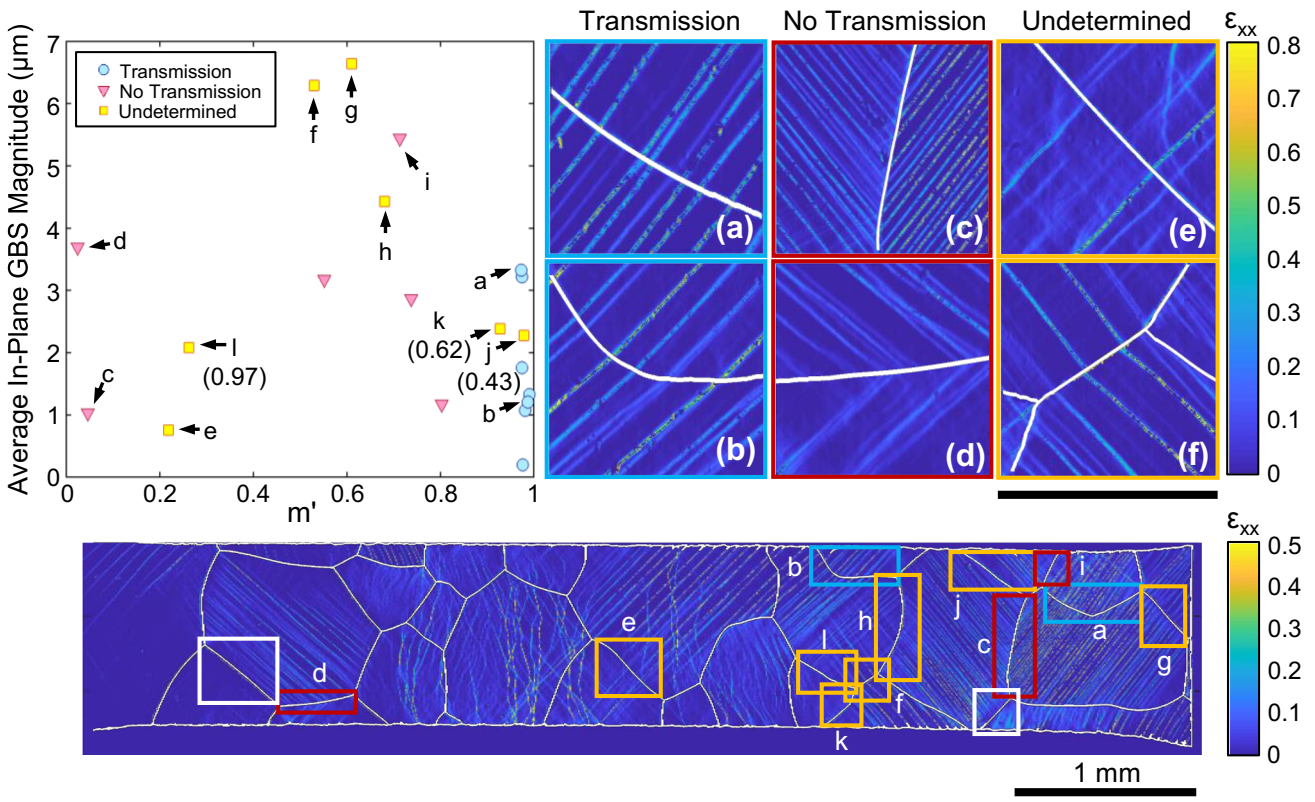

Fig. 11 (Left) Average in-plane GBS magnitude vs. m′ for boundaries with identifiable slip activity in both adjacent grains. Points j, k, and l are labelled with a secondary m′ which could not be discounted due to close similarities in the expected slip trace behavior. (Right) Axial strain fields (ε_{xx}) for several boundary cases: *transmission* in (a) and (b), *no transmission* in (c) and (d), and *undetermined* in (e) and (f). In each case, the grain boundary is highlighted in white and the corresponding data points for each strain field example are marked in the left plot. The black scale bar at the lower right represents the following lengths for each field of view: (a) 160 μm, (b) 200 μm, (c) 330 μm, (d) 200 μm, (e) 200 μm, and (f) 250 μm. (Below) The full gage axial strain field at global axial strain $\varepsilon_7 = 0.046$. The corresponding boundaries for all labelled points in the plot above are highlighted. Unlabeled boundaries boxed in white indicate grain boundaries without sufficient slip activity to calculate m′, and thus not included in average in-plane GBS vs m′ plot, but experienced average in-plane sliding magnitudes above 4 μm

transmission, as defined in Case 2, are in to the lower m′ regime. The highest m′ with no evidence of transmission was 0.8. Despite having spatially aligned traces, there are seven grain boundaries that failed to meet at least one of the two remaining criteria for Case 1 and were classified as Case 3, shown by yellow squares in the plot of Fig. 11. This group spans a large range of m′ values (0.22–0.98) and average in-plane GBS magnitudes (2.1–6.3 μm). Several differences were observed between spatially contiguous slip trace pairs in the Case 1 and Case 3 groups. First, only Case 1 boundaries, which all had m′ values greater than 0.97, appeared to experience many transmission events that were somewhat evenly distributed along the boundary, as seen with boundaries (a) and (b) in Fig. 11. Conversely, this behavior was not observed for any of the Case 3 boundaries. There were never more than one or two contiguous slip trace pairs in question at any of the Case 3 boundaries, which contributed to classification difficulty. Note that the data points in the Fig. 11 plot represent the only grain boundaries of the gage section in Fig. 6 that experienced local slip activity from identifiable slip systems in both adjacent grains and is therefore a small sample set at a specific set of testing conditions. There are several boundaries that did experience relatively large average GBS magnitudes (> 4 μm) and no transmission, including both non-transmission grain boundary-dislocation interactions as well as boundaries experiencing no local slip activity (these boundaries are not included in Fig. 11 plot because slip activity is needed in both adjacent grains to calculate m′), indicating that GBS does not necessarily depend on the occurrence of transmission. However, the three boundaries in the low m′ regime that did experience an average GBS magnitude larger than 5 μm suggest that greater GBS activity may be correlated with slip activity other than high m′ direct slip transmission. Depending on the nature of the slip trace pairs observed at Case 3 boundaries (f) and (g) in Fig. 11, the large GBS activity observed could be interacting with transmission between moderately well aligned slip systems or dislocation emission. A larger data set is required to draw statistically significant conclusions about the possible mechanism correlation trends observed in this experimental work, but it is interesting to note that it has been computationally demonstrated that conditions favorable for GBS can also favor slip transmission. Using

molecular dynamics simulations of coherent twin boundaries in Cu, Sangid et al. observed that increasing shear stress on the grain boundary plane, which is necessary for GBS, decreases the energy barrier for slip transmission [10]. In addition, random high angle grain boundaries, which can enable larger GBS magnitude, shown experimentally in Zn by Kokawa et al. [12], contain greater defect content than low angle and coincident site lattice boundaries and can more efficiently accommodate and relax stresses due to residual dislocations left in the boundary after a transmission event [48]. GBS magnitude has also been directly correlated with increasing grain boundary disorder and energy in atomistic simulations of aluminum bicrystals [49, 50], which conversely suggests an incompatible relationship between GBS and direct transmission resulting in little to no boundary residual, observed to occur at low misorientation [51, 52] and low energy Σ boundaries [53]. In addition to these possible microstructural factors, effects of local stress state variation on GBS/transmission interaction will be explored in future work with crystal plasticity modelling.

The experimental and analytical approaches presented in this work have limitations that should be noted. Although this approach can spatially resolve the extent of GBS and dislocation slip across large mm-scale FOVs, it is a surface measurement. Therefore, the effect of the underlying microstructure is not considered, which was a motivating factor for using a high-purity, columnar specimen despite the inherent experimental difficulties. Additionally, the specimen used in this work was not perfectly columnar (as seen in Fig. 2), which limited the accuracy with which the out of plane component of the boundary plane normal can be determined. The specimen microstructure also exhibited <100> texture due to annealing, which limited the types of boundaries examined. Future studies to investigate grain boundary plastic deformation behavior in columnar microstructures with more randomized textures would provide valuable information regarding mechanism interactions across varied microstructures.

Conclusions

The present work demonstrates an experimental approach to capture high-resolution, large field of view strain and microstructural information in high-purity (99.99%) columnar aluminum subjected to uniaxial tension at 190 °C. Stitched SEM-DIC and EBSD were used to obtain high-resolution strain fields and grain orientation information needed to investigate these mechanisms at grain boundaries across full specimen gages. The resulting 2D measurements of GBS and slip displacements can be used to determine full-gage average values (e.g. contribution of various mechanisms to global strain, average in-plane GBS), spatially resolved deformation behavior (e.g. in-plane GBS magnitude profiles, slip transmission) and globally quantified GBS-slip trends with respect to microstructure (e.g. m vs. GBS magnitude). Several of these analysis approaches have been demonstrated for selected boundaries and for the full specimen microstructure where it was found that: (1) GBS magnitude profiles can have large gradients along a single boundary; (2) GBS magnitude profiles can vary significantly between boundaries; (3)When comparing average in-plane GBS magnitude to m′, two regimes were observed: high m′ ($m' > 0.9$) and low m′ ($m' < 0.9$). All seven grain boundaries that were confidently identified as experiencing direct transmission, as defined by Case 1, fell within the high m′ regime and saw a lower average in-plane GBS than in the low m′ region, but there was no clear direct correlation between these parameters. (4) Two grain boundaries that experience the highest average in-plane sliding magnitude also saw contiguous, yet undetermined slip trace pairs, suggesting a possible interaction between GBS and slip transmission or dislocation emission; future work is needed to examine statistically significant numbers of grain boundaries at varied test conditions. While the characterization of m′ and averaged GBS magnitude gives insight into the relationship between GBS and slip transmission, further investigation including local microstructural effects is warranted. Future study of this mechanism relationship will consider additional microstructural parameters and take advantage of spatially-resolved, large field of view microstructure and strain information made possible by this approach to characterize complex deformation trends with respect to the GBS-slip transmission mechanism relationship.

Acknowledgements This work was supported by the United States Department of Energy, Office of Basic Energy Sciences, Division of Materials Sciences and Engineering under Awards #DE-SC-0013971 and #DE-SC-0014281. The authors gratefully acknowledge Dr. Zhe Chen for his scientific advice and for sharing codes for image and displacement/strain field stitching; Mr. Chris Torbet for helpful scientific discussions, and for his generous assistance in electrical discharge machining of test specimens; Mr. David Bothman for helpful specimen preparation suggestions; and Mr. Mark Cornish and Mr. Darin Randall for helpful discussions and assistance regarding scanning electron microscopy.

References

1. Sutton AP, Balluffi RW (2006) Interfaces in Crystalline Materials. Oxford University Press, Oxford
2. Shen Z, Wagoner RH, Clark WAT (1988) Dislocation and grain boundary interactions in metals. Acta Metall 36:3231–3242. https://doi.org/10.1016/0001-6160(88)90058-2
3. Lee TC, Robertson IM, Birnbaum HK (1989) Anomalous slip in an FCC system. Ultramicroscopy 29:212–216. https://doi.org/10.1016/0304-3991(89)90248-9
4. Lee TC, Robertson IM, Birnbaum HK (1990) An *In Situ* transmission electron microscopy deformation study of the slip transfer

mechanisms in metals. Metall Trans A 21:2437–2447. https://doi.org/10.1007/BF02646988
5. Livingston JD, Chalmers B (1957) Multiple slip in bicrystal deformation. Acta Metall 5:322–327. https://doi.org/10.1016/0001-6160(57)90044-5
6. Spearot DE, Sangid MD (2014) Insights on slip transmission at grain boundaries from atomistic simulations. Curr Opin Solid St M 18:188–195. https://doi.org/10.1016/j.cossms.2014.04.001
7. Yamakov V, Wolf D, Phillpot SR, Mukherjee AK, Gleiter H (2004) Deformation-mechanism map for nanocrystalline metals by molecular-dynamics simulation. Nat Mater 3:43–47. https://doi.org/10.1038/nmat1035
8. Vo NQ, Averback RS, Bellon P, Odunuga S, Caro A (2008) Quantitative description of plastic deformation in nanocrystalline Cu: Dislocation glide versus grain boundary sliding. Phys Rev B 77:134108. https://doi.org/10.1103/PhysRevB.77.134108
9. Sangid MD, Ezaz T, Sehitoglu H, Robertson IM (2011) Energy of slip transmission and nucleation at grain boundaries. Acta Mater 59:283–296. https://doi.org/10.1016/j.actamat.2010.09.032
10. Sangid MD, Ezaz T, Sehitoglu H (2012) Energetics of residual dislocations associated with slip-twin and slip-GBs interactions. Mater Sci Eng A 542:21–30. https://doi.org/10.1016/j.msea.2012.02.023
11. Raman V, Langdon TG (1990) Cyclic Grain Boundary Migration and Sliding in Pure Aluminum. Acta Metall Mater (3):497–507. https://doi.org/10.1016/0956-7151(90)90156-B
12. Kokawa H, Watanabe T, Karashima S (1981) Sliding behaviour and dislocation structures in aluminium grain boundaries. Philos Mag A 44:1239–1254. https://doi.org/10.1080/01418618108235806
13. Kumar K, Van Swygenhoven H, Suresh S (2003) Mechanical behavior of nanocrystalline metals and alloys. Acta Mater 51:5743–5774. https://doi.org/10.1016/j.actamat.2003.08.032
14. Mompiou F, Legros M, Bóe A, Coulombier M, Raskin JP, Pardoen T (2013) Inter- and intragranular plasticity mechanisms in ultrafine-grained Al thin films: An *in situ* TEM study. Acta Mater 61:205–216. https://doi.org/10.1016/j.actamat.2012.09.051
15. Langdon TG (2006) Grain boundary sliding revisited: Developments in sliding over four decades. J Mater Sci 41:596–609. https://doi.org/10.1007/s10853-006-6476-0
16. Langdon TG (1994) A unified approach to grain boundary sliding in creep and superplasticity. Acta Metall Mater 42:2437–2443. https://doi.org/10.1016/0956-7151(94)90322-0
17. Cahn JW, Mishin Y, Suzuki A (2006) Coupling grain boundary motion to shear deformation. Acta Mater 54:4953–4975. https://doi.org/10.1016/j.actamat.2006.08.004
18. Schiotz J, Di Tolla FD, Jacobsen KW (1998) Softening of nanocrystalline metals at very small grain sizes. Nature 391:561–563. https://doi.org/10.1038/35328
19. Van Swygenhoven H, Spaczer M, Caro A, Farkas D (1999) Competing plastic deformation mechanisms in nanophase metals. Phys Rev B 60:22–25. https://doi.org/10.1103/PhysRevB.60.22
20. Van Swygenhoven H, Derlet P (2001) Grain-boundary sliding in nanocrystalline fcc metals. Phys Rev B 64:224105. https://doi.org/10.1103/PhysRevB.64.224105
21. Sauvage X, Wilde G, Divinski SV, Horita Z, Valiev RZ (2012) Grain boundaries in ultrafine grained materials processed by severe plastic deformation and related phenomena. Mater Sci Eng A 540:1–12. https://doi.org/10.1016/j.msea.2012.01.080
22. Sabirov I, Murashkin MY, Valiev RZ (2013) Nanostructured aluminum alloys produced by severe plastic deformation: New horizons in development. Mater Sci Eng A 560:1–24. https://doi.org/10.1016/j.msea.2012.09.020
23. Kammers AD, Wongsa-Ngam J, Langdon TG, Daly S (2014) The effect of microstructure heterogeneity on the microscale deformation of ultrafine-grained aluminum. J Mater Res 29:1664–1674. https://doi.org/10.1557/jmr.2014.207
24. Moore HF, Betty BB, Dollins CW (1935) The creep and fracture of lead and lead alloys. University of Illinois Bulletin 32:9–50
25. Valiev RZ, Kaibyshev OA, Astanin VV, Emaletdinov AK (1983) The nature of grain boundary sliding and the superplastic flow. Phys Status Solidi 78:439–448. https://doi.org/10.1002/pssa.2210780209
26. Bourcier M, Bornert M, Dimanov A, Héripré E, Raphanel JL (2013) Multiscale experimental investigation of crystal plasticity and grain boundary sliding in synthetic halite using digital image correlation. J Geophys Res Solid Earth 118:511–526. https://doi.org/10.1002/jgrb.50065
27. Carter JLW, Kuper MW, Uchic MD, Mills MJ (2014) Characterization of localized deformation near grain boundaries of superalloy René-104 at elevated temperature. Mater Sci Eng A 605:127–136. https://doi.org/10.1016/j.msea.2014.03.048
28. Doquet V, Barkia B (2016) Combined AFM, SEM and crystal plasticity analysis of grain boundary sliding in titanium at room temperature. Mech Mater 103:18–27. https://doi.org/10.1016/j.mechmat.2016.09.001
29. Zhao Y, Toth L, Massion R, Skrotzki W (2018) Role of Grain Boundary Sliding in Texture Evolution for Nanoplasticity. Eng Mater 20:1700212. https://doi.org/10.1002/adem.201700212
30. Bieler T, Mukherjee A (1990) The High Strain Rate Superplastic Deformation Mechanisms of Mechanically Alloyed Aluminum IN90211. Mater Sci Eng A 128:171–182. https://doi.org/10.1016/0921-5093(90)90225-R
31. Horton CAP (1970) Some effects of solid solution additions of copper on grain boundary sliding in aluminium. Acta Metall 18:1159–1168. https://doi.org/10.1016/0001-6160(70)90106-9
32. Huang K, Logé RE (2016) A review of dynamic recrystallization phenomena in metallic materials. J Mater Des 111:548–574. https://doi.org/10.1016/j.matdes.2016.09.012
33. Kassner ME (1987) Large-Strain Deformation of Aluminum Single Crystals at Elevated Temperature as a Test of the Geometric-Dynamic-Recrystallization Concept. Metall Trans A 20A:2182–2185. https://doi.org/10.1007/BF02650307
34. Ravichandran N, Prasad YVRK (1991) Dynamic Recrystallization during Hot Deformation of Aluminum: A Study Using Processing Maps. Metall Trans A 22A:2339–2348. https://doi.org/10.1007/BF02665000
35. Kammers AD, Daly S (2013) Self-Assembled nanoparticle surface patterning for improved digital image correlation in a scanning electron microscope. Exp Mech 53:1333–1341. https://doi.org/10.1007/s11340-013-9734-5
36. Sutton MA, Li N, Garcia D, Cornille N, Orteu JJ, McNeill SR, Schreier HW, Li X (2006) Metrology in a scanning electron microscope: theoretical developments and experimental validation. Meas Sci Technol 17:2613–2622. https://doi.org/10.1088/0957-0233/17/10/012
37. Sutton MA, Orteu JJ, Schreier HW (2009) Image Correlation for Shape, Motion and Deformation Measurements. Springer, New York
38. Chen Z, Lenthe W, Stinville JC, Echlin M, Pollock T, Daly S (2018) High-Resolution Deformation Mapping Across Large Fields of View using Scanning Electron Microscopy and Digital Image Correlation. Exp Mech 58:1407–1421
39. Doherty PE, Davis RS (1963) Direct Observation of Oxidation of Aluminum Single-Crystal Surfaces. J Appl Phys 1963:34;619–34;628. https://doi.org/10.1063/1.1729318
40. Jeurgens LPH, Sloof WG, Tichelaar FD, Mittemeijer EJ (2002) Growth kinetics and mechanisms of aluminum-oxide films formed by thermal oxidation of aluminum. J Appl Phys 92:1649–1656. https://doi.org/10.1063/1.1491591
41. Linne MA, Daly S (2019) Data Clustering for High-Resolution Alignment of Microstructure and Strain Fields (Submitted)

42. Valiev RZ, Gertsman VY, Kaibyshev OA (1989) Grain Boundary Structure and Properties under External Influences. Phys Status Solidi 97:11–56. https://doi.org/10.1002/pssa.2210970102
43. Bourdin F, Stinville JC, Echlin MP, Callahan PG, Lenthe WC, Torbet CJ, Texier D, Bridier F, Cormier J, Villechaise P, Pollock TM, Valle V (2018) Measurements of plastic localization by heaviside-digital image correlation. Acta Mater 157:307–325. https://doi.org/10.1016/j.actamat.2018.07.013
44. Mussot P, Rey C, Zaoui A (1985) Grain Boundary Sliding and Strain Compatibility. Res Mech 14:69–79
45. Luster J, Morris MA (1995) Compatibility of Deformation in Two-Phase Ti-Al alloys: Dependence on Microstructure and Orientation Relationships. Metall Mater Trans A 26:1745–1756. https://doi.org/10.1007/BF02670762
46. Bieler TR, Eisenlohr P, Zhang C, Phukan HJ, Crimp MA (2014) Grain boundaries and interfaces in slip transfer. Curr Opinion Solid State Mater Sci 18:212–226. https://doi.org/10.1016/j.cossms.2014.05.003
47. Chen Z, Daly SH (2017) Active slip system identification in polycrystalline metals by digital image correlation (DIC). Exp Mech 57:115–127. https://doi.org/10.1007/s11340-016-0217-3
48. Hirth JP, Lothe J (1968) Theory of Dislocations. McGraw-Hill, New York
49. Namilae S, Chandra N, Nieh TG (2002) Atomistic simulation of grain boundary sliding in pure and magnesium doped aluminum bicrystals. Scr Mater 46:59–54. https://doi.org/10.1016/S1359-6462(01)01195-2
50. Qi Y, Krajewski PE (2007) Molecular dynamics simulations of grain boundary sliding: The effect of stress and boundary misorientation. Acta Mater 55:1555–1563. https://doi.org/10.1016/j.actamat.2006.10.016
51. Zaefferer S, Kuo JC, Zhao Z, Winning M, Raabe D (2002) On the influence of grain boundary misorientation on the plastic deformation of aluminum bicrystals. Acta Mater 51:4719–4735. https://doi.org/10.1016/S1359-6454(03)00259-3
52. Kobayashi S, Tsurekawa S, Watanabe T (2005) Grain boundary hardening and triple junction hardening in polycrystalline molybdenum. Acta Mater 53:1051–1057. https://doi.org/10.1016/j.actamat.2004.11.002
53. Lim LC, Raj R (1985) The role of residual dislocation arrays in slip induced cavitation, migration and dynamic recrystalization at grain boundaries. Acta Metall 12:2205–2214. https://doi.org/10.1016/0001-6160(85)90182-8

Publisher's Note Springer Nature remains neutral with regard to jurisdictional claims in published maps and institutional affiliations.